

# Combined optical and acoustical detection of single microbubble dynamics

Jeroen Sijl

*Physics of Fluids Group and MIRA Institute of Biomedical Technology and Technical Medicine,  
University of Twente, P.O. Box 217, 7500 AE Enschede, The Netherlands*

Hendrik J. Vos

*Biomedical Engineering, Erasmus MC, P.O. Box 2040, 3000 CA Rotterdam, The Netherlands*

Timo Rozendaal

*Physics of Fluids Group, University of Twente, P.O. Box 217, 7500 AE Enschede, The Netherlands*

Nico de Jong

*Biomedical Engineering Department, Erasmus MC, P.O. Box 2040, 3000 CA Rotterdam, The Netherlands*

Detlef Lohse and Michel Versluis<sup>a)</sup>

*Physics of Fluids Group and Institute of Biomedical Technology and Technical Medicine MIRA,  
University of Twente, P.O. Box 217, 7500 AE Enschede, The Netherlands*

(Received 9 December 2010; revised 18 May 2011; accepted 19 May 2011)

A detailed understanding of the response of single microbubbles subjected to ultrasound is fundamental to a full understanding of the contrast-enhancing abilities of microbubbles in medical ultrasound imaging, in targeted molecular imaging with ultrasound, and in ultrasound-mediated drug delivery with microbubbles. Here, single microbubbles are isolated and their ultrasound-induced radial dynamics recorded with an ultra-high-speed camera at up to 25 million frames per second. The sound emission is recorded simultaneously with a calibrated single element transducer. It is shown that the sound emission can be predicted directly from the optically recorded radial dynamics, and vice versa, that the nanometer-scale radial dynamics can be predicted from the acoustic response recorded in the far field. © 2011 Acoustical Society of America.

[DOI: 10.1121/1.3626155]

PACS number(s): 43.80.Qf, 43.35.Yb, 43.80.Vj, 43.35.Ei [CCC]

Pages: 3271–3281

## I. INTRODUCTION

Microbubbles are used as contrast agents for medical ultrasound imaging.<sup>1</sup> With a mean bubble radius between 1 and 5 μm the bubbles are resonant scatterers at typical medical ultrasound frequencies of 1–6 MHz. The bubbles scatter ultrasound more efficiently than a solid particle of the same size, at up to 9 orders of magnitude, owing primarily to the compressibility of the gas.<sup>2</sup> In addition, microbubbles scatter ultrasound nonlinearly at harmonic frequencies of the driving frequency. The nonlinear acoustic response of the bubbles allows for a discrimination from the linear tissue echo, thereby improving the contrast-to-tissue ratio and forming the basis for the development of harmonic imaging methods, including power modulation imaging,<sup>3</sup> and pulse inversion imaging.<sup>4</sup> Contrast agent microbubbles, unlike tissue, are also seen to emit energy at the one-half subharmonic frequency of the driving frequency, which may favor detection.<sup>5–9</sup> More recent applications of microbubbles are in molecular targeting and in sonoporation.<sup>1,10</sup> In molecular targeting applications ligands are attached to the bubble coating and bind to specific markers expressed by diseased cells. In sonoporation applications the cell membrane opens

momentarily as a result of the local stress exerted by bubble oscillations and jets.<sup>11,12</sup> The transient opening of the cell membrane facilitates drug uptake by the cell.

In order to predict the nonlinear echoes from microbubbles, necessary for the optimization of contrast detection methods, detailed knowledge is needed on the physical origin of these echoes. Simply stated, microbubbles are excited by the transmitted pulse into an oscillation, which in turn converts into an acoustic response received by the ultrasound system. This path is schematically represented in Fig. 1. The first part of the path determines the bubble dynamics in response to the driving pressure pulse. In the case of spherical oscillations, or volumetric oscillations, the dynamics of the bubble is described by the radius-time curve  $R(t)$ . For an uncoated bubble in an unbounded medium the relation between the driving pressure and the dynamic response is well described by the Rayleigh–Plesset (RP) equation.<sup>13–15</sup> The RP equation is an ordinary nonlinear differential equation. In linearized form, i.e., for small radial excursions, it takes the analytical form of a harmonic oscillator.<sup>14,15</sup> For larger radial excursions (on the order of 10% and higher) a nonlinear relation between the driving pressure wave and the radial response exists, and therefore the radial dynamics can contain higher-harmonic and subharmonic frequency components of the fundamental driving frequency.<sup>14–16</sup>

<sup>a)</sup>Author to whom correspondence should be addressed. Electronic mail: m.versluis@utwente.nl

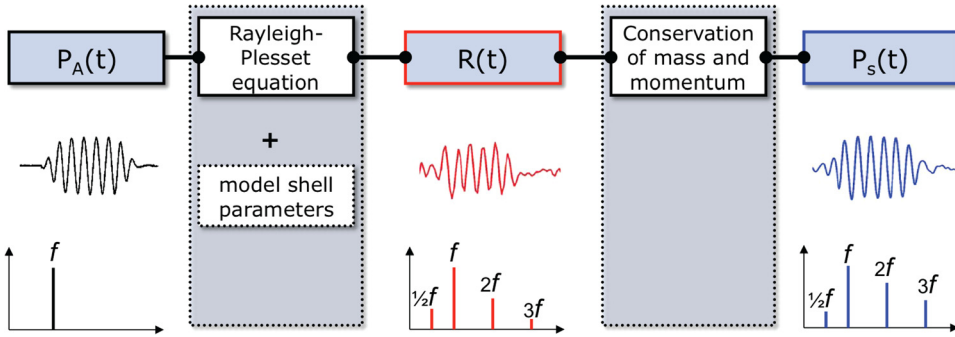


FIG. 1. (Color online) A schematic view on the origin of ultrasound scattering of a single coated microbubble.  $P_A(t)$  is the driving pressure,  $R(t)$  is the radial response of the microbubble, and  $P_s(t)$  the resulting echo response.

To stabilize medical ultrasound contrast microbubbles the interface is coated with a protein, lipid, or polymer layer, which resists gas diffusion and decreases surface tension. The coating can introduce additional linear and nonlinear components to the dynamic response. The dilatational viscosity of the shell material results in an overall damping of the oscillation, while the elasticity of the shell material results in an increase of the resonance frequency.<sup>17</sup> Moreover, the viscoelastic properties can become nonlinear, which adds to the intrinsic nonlinear features of the bubble dynamics. The influence of a viscoelastic coating has been extensively studied theoretically and experimentally, see, e.g., Refs. 8, 9, 18–26. In general, the RP equation is extended to model the contributions of the shell. The viscoelastic properties are then captured by a set of shell parameters, whose values can be determined experimentally. A possible experimental approach would be to optically record the radial dynamics of a microbubble for a set of ultrasound parameters, notably pressure and frequency, from which the shell parameters are extracted by comparing the experimental curves with those of the theoretical predictions.<sup>27</sup>

The second part of the path depicted in Fig. 1, the conversion from radial excursion to the scattered sound wave  $P_s(t)$ , has had far less attention in literature. The theoretical derivation is based on conservation of mass and momentum<sup>2,14</sup> and the final equation has been used in literature to predict the echo from experimentally or numerically obtained radial dynamics.<sup>2,14,25,28,29</sup> The conversion of the pulsating bubble volume into acoustic energy depends on the geometrical size of the bubble, and the velocity and the acceleration of the bubble wall. The exact relation will be given in Sec. II. Only a few studies hint at the implications of the conversion.<sup>25,30</sup> The equation assumes the bubble to be isolated in an infinite medium and the bubble to remain spherical at all times. From *in vitro*, *ex vivo*, and *in vivo* studies it is known that bubbles are located in confined geometries, which leads to interactions with adjacent walls.<sup>31–35</sup> Neighboring bubbles are acoustically coupled. For molecular imaging applications, microbubbles are targeted to diseased cells through ligands introducing complex biomolecular interactions. These interactions may also lead to nonspherical bubble oscillations. In conclusion, *a priori* it is not known whether the echo of a pulsating microbubble can be predicted from an experimental radius vs time curve. Furthermore, the implications of the conversion have not been described in detail before.

Studying the applicability of the conversion requires simultaneous recordings of both the radial response  $R(t)$  and

the resulting acoustic response  $P_s(t)$  of a microbubble. Here we present a detailed experimental investigation of the different contributions to the overall acoustic response of coated microbubbles. We employ the ultra-high-speed camera Brandaris 128 (Ref. 36) to resolve the radial dynamics of a single microbubble and combine the results with a sensitive and calibrated acoustic setup to quantitatively assess its acoustic response. Through this combined setup we can monitor both the bubble dynamics and the emitted sound and verify the degree of correspondence of the signals. The data are also used to investigate the estimation of the radial dynamics of the bubble explicitly from its acoustic signature and resting radius. This reverse calculation is nontrivial and to our knowledge has never been described in the context of ultrasound contrast agents.

## II. THEORY

The scattering of an incident ultrasound field by an oscillating microbubble consists of two contributions.<sup>2</sup> The first is a passive contribution that results from the perturbation in the compressibility of the propagating medium (that may originate from any body, oscillating or not) and the second is an active contribution that results from the volumetric oscillations of the bubble. In regular applications, ultrasound contrast microbubbles are gaseous and much smaller than the incident field wavelength, which implies that the passive contribution can be safely neglected as shown previously by Hilgenfeldt *et al.*<sup>2</sup>

The active contribution to the scattered ultrasound field is determined by the radial dynamics of the microbubble, described by  $R(t)$ . The microbubble is assumed to be spherical at all times. From conservation of mass and momentum it follows that the emitted pressure wave  $P_s(r, t)$  at distance  $r$  is determined from the second time derivative of the volume  $V(t)$  of the bubble, see, e.g., Refs. 2, 14, and 37,

$$\hat{P}_s(r, t - r/c) = \frac{1}{4\pi r} \hat{V}(t) = \frac{1}{3} \frac{\rho}{r} \frac{\partial^2}{\partial t^2} [R(t)^3], \quad (1)$$

where  $c$  denotes the speed of sound in the medium ( $\approx 1500$  m/s in water) and  $\rho$  is the density of the surrounding liquid ( $\approx 10^3$  kg/m<sup>3</sup> for water). It is assumed that the receiver is sufficiently far from the microbubble ( $r \gg R$ ) to neglect the Bernoulli pressure, also referred to as the kinetic wave, which decreases with  $1/r^4$ . The finite time for the pressure wave to travel a distance  $r$  from the bubble wall to the transducer surface is accounted for by the term  $r/c$ . We write  $\hat{P}_s$

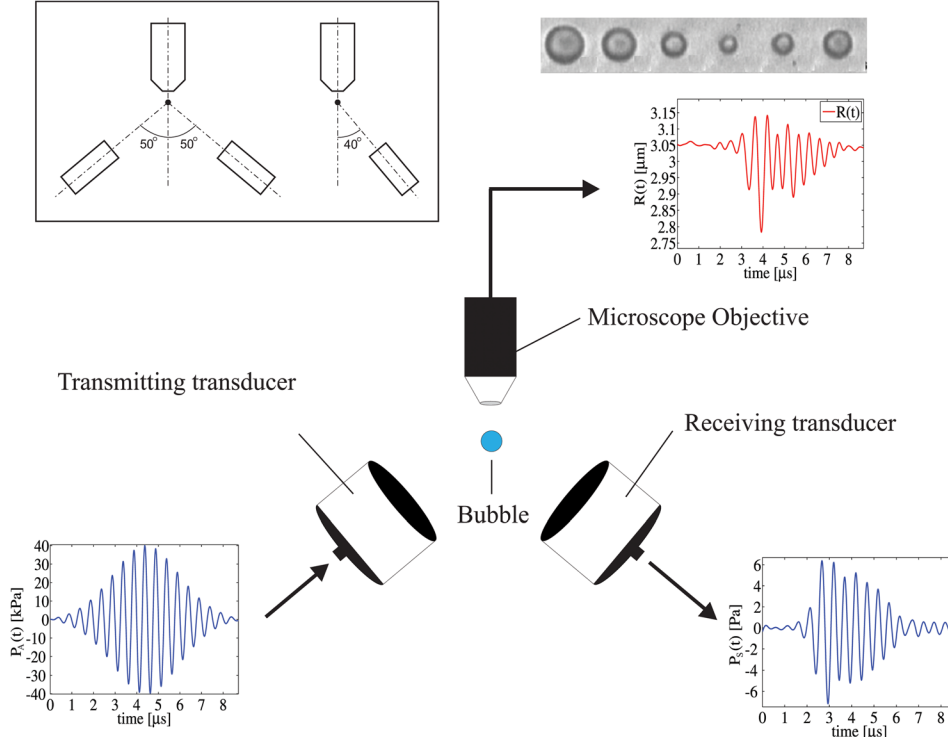


FIG. 2. (Color online) A schematic view of the setup. A Gaussian-apodized driving pressure waveform was transmitted by a focused ultrasound transducer. The echo response of the bubble was received by a second focused calibrated transducer. Simultaneously, the radial dynamics of the microbubble was recorded through a  $100\times$  microscope objective connected to the Brandaris-128 ultra-high-speed camera (Ref. 36). The inset at the top-left corner shows in two side views the positioning of the transducers with respect to the microscope objective.

when the pressure is derived from the radial or volumetric motion of the microbubble, and  $P_s$  when the pressure is measured directly.

In order to understand the effect of Eq. (1) on the bubble echo it is insightful to linearize Eq. (1). For this purpose we assume the radial dynamics to be described by  $R(t) = R_0\{1 - \epsilon \sin(\omega t)\}$ , where  $\epsilon \ll 1$  is the relative radial excursion and  $\omega$  is the angular frequency of the oscillation. The initial bubble radius is given by  $R_0$ . Inserting this into Eq. (1) and ignoring terms of second and higher order yields

$$\hat{P}_s(r, t - r/c) = \frac{\rho \omega^2 R_0^3 \epsilon \sin(\omega t)}{r} \quad (2)$$

First, this relation shows that the amplitude of the scattered sound of the bubble increases with the third power of the initial bubble radius. Second, the amplitude of the scattered sound of an oscillating bubble increases quadratically with the frequency of oscillation. This is a result of the second time derivative in Eq. (1). If the microbubble radial response contains higher harmonics of the driving pulse, then the echo amplitude of these harmonics will be enhanced with respect to the fundamental echo amplitude of the driving pulse. For example, the echo amplitude of the second harmonic is enhanced by a factor of 4 compared to the fundamental echo amplitude.

Several assumptions are made in the derivation of Eq. (1). We consider an isolated single bubble in an infinite medium and exclude wall reflections and sound emission from neighboring pulsating bubbles. Furthermore, Eq. (1) accounts only for volumetric oscillations of the bubble; we will validate later that nonspherical oscillations, or surface modes, do not contribute significantly to the sound emission. Translation of the bubble as a result of the acoustic driving

also contributes to the sound scattering.<sup>2,38</sup> However, this contribution is of the same order as that of the passive contribution and can therefore be neglected.<sup>2</sup>

### III. EXPERIMENTAL SETUP

To investigate the applicability of Eq. (1) we combined the Brandaris-128 ultra-high-speed camera<sup>36</sup> with an acoustic setup capable of quantitatively recording the sound transmitted by a single oscillating microbubble. The combined setup is schematically shown in Fig. 2. Microbubbles are confined in a  $200\text{ }\mu\text{m}$  diameter cellulose capillary tube with a wall thickness of  $8\text{ }\mu\text{m}$  (Product No. 132294, Spectrum Europe, Breda, The Netherlands). The capillary tube was mounted horizontally in a cylindrical Plexiglas water-filled container that also supports the acoustic parts. The contrast agent studied was BR-14 (Bracco Research S.A., Geneva, Switzerland), an experimental contrast agent containing microbubbles with a phospholipid coating and a perfluorocarbon gas core.

#### A. Single bubble selection

It is not straightforward to ensure that the acoustic response received by the transducer results from a single microbubble. It requires the isolation of a microbubble with an initial bubble radius of around  $2\text{ }\mu\text{m}$  in a volume as large as  $2\text{ mm}^3$  (i.e., dimensions comparable to the wavelength of the ultrasound and focal region of the used transducers). We have achieved the isolation with the use of a micropipette. With reference to Fig. 3, a microbubble suspension was injected into a small reservoir. On one side the reservoir was connected to the capillary tube that leads to the measurement section. The capillary tube entered the bubble reservoir  $400\text{ }\mu\text{m}$  below the top surface of the reservoir; this prevented

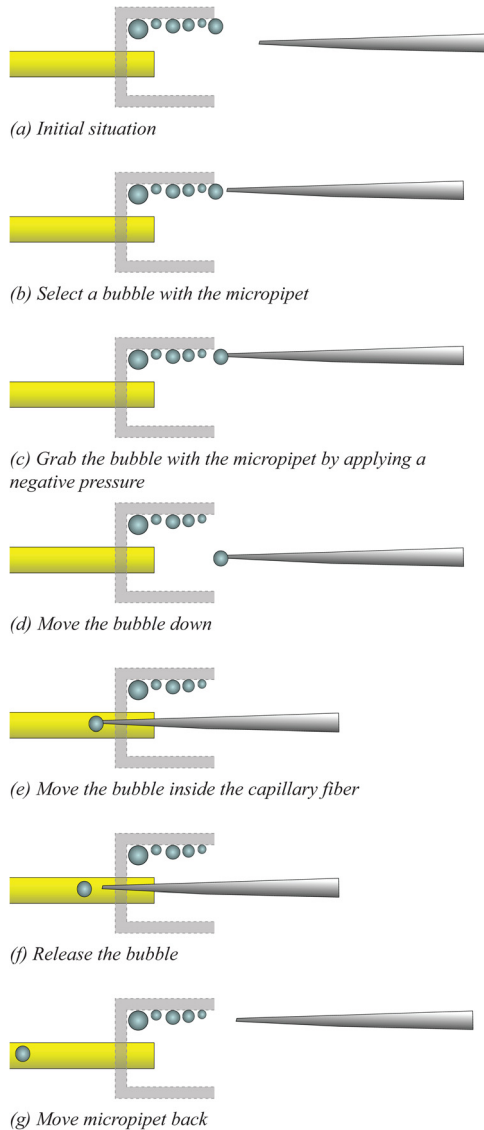


FIG. 3. (Color online) Schematic of the bubble selection and isolation method using a translating micropipette.

bubbles that are touching the top surface from flowing into the tube. The other side of the bubble reservoir was open to the atmosphere, but nevertheless capillary forces prevented the solution from flowing out. A micropipette that was mounted on a three-dimensional-translation stage entered the bubble reservoir from the open side. The micropipette had a tip size of  $0.5 \mu\text{m}$ , which is smaller than the bubble size. A single bubble was grabbed by applying a negative pressure with a syringe connected to the pipette. Then the bubble was brought down into the capillary tube and released.<sup>39</sup> With a syringe pump connected to the other side of the capillary tube we moved the bubble through the capillary tube into the measurement section. Note that the bubble remains in the capillary tube during the experiments.

## B. Acoustic setup

A 2 MHz center frequency transducer (PA168, PVDF-type, diameter 18 mm, focus 22 mm, 100% –6 dB relative

bandwidth, Precision Acoustics Ltd., Dorset, UK) was used to excite the bubble with an ultrasound pulse. A second transducer (C381-1 in. focus, 3.5 MHz, 100% –6 dB relative bandwidth, Panametrics, Olympus NDT, Waltham, MA) received the acoustic bubble response. The transducers were aligned in the same plane of the capillary tube under an angle of  $50^\circ$  to the capillary tube and at a  $100^\circ$  angle to each other in order to minimize specular reflection of the driving ultrasound on the capillary, see the inset at the top-left corner of Fig. 2. Two calibrated 0.2 mm needle hydrophones (Precision Acoustic Ltd., Dorset, UK) were mounted in the Plexiglas container exactly opposite to the two transducers. The hydrophones could be moved in and out of the focus of the two transducers and were used to confocally align the two transducers with the microscope objective. The transmit transducer was excited with pulses generated by an arbitrary waveform generator (AWG 8026, Tabor Electronics Ltd., Tel Hanan, Israel) and amplified by a linear power amplifier (350L, ENI, Rochester, NY). The received bubble echoes were amplified 59.3 dB by a low-noise amplifier (AU-1519-10289, Miteq, Hauppauge, NY) and digitized by a digital oscilloscope (TDS 3012, Tektronix, Beaverton, OR). The digitized data were stored on a personal computer through a general-purpose interface bus-link for off-line analysis. Gaussian-apodized driving pressure pulses with frequencies ranging from 1 to 4 MHz were used to excite the bubbles. All pulses had a peak negative pressure amplitude of 40 kPa and had a length of  $8.9 \mu\text{s}$ . The output of the transducer was calibrated with a calibrated hydrophone. The accuracy of the calibration procedure was  $\pm 10\%$ , which corresponds to  $\pm 0.8 \text{ dB}$ .

## C. Optical setup

A  $100\times$  magnification microscope objective (LUMFPL  $100\times/W$ , NA = 1.0, Olympus, Tokyo, Japan) connected to an upright microscope (BX-FM, Olympus) was focused in the combined acoustical focus of the two focused transducers. The focal distance of the objective was 1.1 mm. In the experiments described here the Brandaris 128 camera recorded a series of six movies of 128 frames each at a frame rate near  $15 \times 10^6$  frames/s. The time interval between the recordings was 2.5 s. The microbubble was illuminated from below with a high-intensity xenon flashlight (MVS 7010 XE, Perkin Elmer, Waltham, MA). A continuous light source (ACE I, Schott, NY) in combination with a single CCD video camera (LCL-902K, Watec, Qwonn) was used to monitor the bubble in between experiments.

## D. Data processing

The measured voltage–time curves were converted into pressure–time curves using the calibrated receive transfer function of the transducer following the procedure described by Sijl *et al.*<sup>22</sup> The setup, including the capillary tube, reflects the transmitted ultrasound pulse, thereby producing an offset in the acoustic response. For each experiment the background signal was recorded in the absence of a microbubble and subtracted from the signal recorded in the presence of a microbubble.

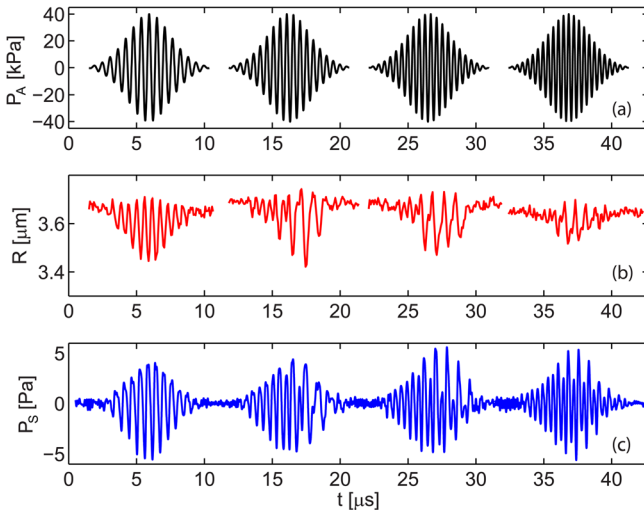


FIG. 4. (Color online) A typical example of the combined optical (b) and acoustical (c) detection of the dynamics of an isolated  $3.7 \mu m$  bubble. Driving pressure pulses had a frequency of 1.7, 2, 2.3, and 2.6 MHz, respectively (a).

The optical frames were analyzed to obtain the  $R(t)$  curves through a semiautomatic minimum cost algorithm<sup>21</sup> in MATLAB (The Mathworks, Natick, MA). A second order finite difference equation was used to calculate the second time derivative of  $R^3[n]$ ,  $n$  being the frame number,

$$\frac{\partial^2}{\partial t^2} [R(t)^3] \approx \frac{R^3[n+1] - 2R^3[n] + R^3[n-1]}{\Delta t^2}. \quad (3)$$

#### IV. RESULTS

A total of 16 different microbubbles were studied at varying radii and frequencies, resulting in a set of 194 recordings. The initial bubble radius ranged from 1.4 to  $6.7 \mu m$ . Depending on the initial bubble radius and the driving frequency, bubbles were observed to oscillate nonlinearly, i.e., when a higher-harmonic or subharmonic component could be identified in the radius-time curve. Figure 4 shows a typical recording of the response of an isolated bubble of  $3.7 \mu m$  radius to pulses with an increasing frequency of 1.7–2.7 MHz [Fig. 4(a)]. The optically recorded radial responses are shown in Fig. 4(b). At the lowest driving frequency (left hand side) the bubble follows the driving pressure pulse, except that it displays the so-called “compression-only” behavior. The compression-only behavior was first described by de Jong *et al.*,<sup>40</sup> where it was observed that the bubbles compress efficiently while their expansion is suppressed. Compression-only behavior occurs when the surface of the bubble is fully saturated with phospholipids and the bubble reaches a tensionless state. Upon compression, the phospholipid coating then easily tends to buckle. A detailed theoretical understanding of the source of this nonlinear behavior was provided very recently by Sijl *et al.*<sup>41</sup> through a weakly nonlinear analysis of the shell buckling model proposed by Marmottant *et al.*<sup>18</sup> At higher driving frequencies a strong subharmonic component develops after a few cycles of the driving pulse.<sup>9</sup> The amplitude of the

radial excursion decreases with increasing frequency, which is expected for bubbles that are driven with frequencies increasingly higher than the resonance frequency. The simultaneously recorded acoustic response [Fig. 4(c)] shows similar envelopes as the driving pulse, and also shows the subharmonic component, although at lesser extent than in the optical data; this effect will be extensively addressed later.

#### A. Linear response

A typical example of the recorded oscillations of a  $6.5 \mu m$  bubble subject to a 1 MHz, 40 kPa driving pulse is shown in Fig. 5(a). The camera recorded at a frame rate of  $12.5 \times 10^6$  frames/s. From the absence of higher harmonics in the spectra of the  $R(t)$  curve shown in Fig. 5(b), we conclude that the oscillations are a linear response to the driving pulse. With Eq. (1) and the experimentally determined  $R(t)$  curve we have calculated the resulting  $\hat{P}_s(t)$ , see Fig. 5(c). The distance  $r$  in Eq. (1) was taken equal to 2.6 cm, the distance to the receiving transducer.

The higher frequency content in the  $R(t)$  curve is enhanced in the calculated  $\hat{P}_s(t)$  curve by a factor  $\omega^2$ , see Eq. (2). The noise content on the  $R(t)$  curve determined from the high-speed recording is around 35 dB lower than the fundamental response, as can be appreciated in Fig. 5(b). Because of the  $\omega^2$  dependence, the high-frequency noise level in the calculated pressure curve can become as high as the bubble response signal, see Fig. 5(d). In the time trace  $\hat{P}_s(t)$  the fundamental frequency response is barely visible because of high-frequency noise.

Figure 5(e) shows the predicted  $\hat{P}_s(t)$  in the same graph as the actually measured pressure-time curve  $P_s(t)$ .  $P_s(t)$  was obtained from the inverse Fourier transform of  $P_s(\omega)$ , where  $P_s(\omega)$  is the product of the Fourier transform of the pressure amplitude-time curve (as measured with the receiving transducer) and the frequency transfer function of the transducer. To compare the curves in the time domain a low-pass fourth order Butterworth filter with a cut-off frequency of 2 MHz was applied to the predicted  $\hat{P}_s(t)$  curve to reduce noise. The agreement is remarkable since the curves are obtained with two independent measurement methods. Interestingly, both the acoustic setup and the optical setup in combination with Eq. (1) are able to pick up and correctly predict pressure variations on the order of 1 Pa on top of an ambient pressure of  $10^5$  Pa. Moreover, the agreement is excellent also in absolute pressure.

In Fig. 5(f) the normalized power spectrum of the calculated and low-pass filtered  $\hat{P}_s(t)$  curve and the power spectrum of the measured pressure curve are shown. The agreement between the two curves around the driving frequency is very good, consistent with the agreement found in time domain between the two curves.

The above-shown data processing for a single bubble was repeated for all recordings. The traces were bandpass filtered to keep the frequency content at the fundamental driving frequency, and the maximum amplitude of oscillation was found by using a Hilbert transform to calculate the envelope of oscillation. The amplitudes of all echoes are shown in the scatter plot in Fig. 6. The solid line denotes equal

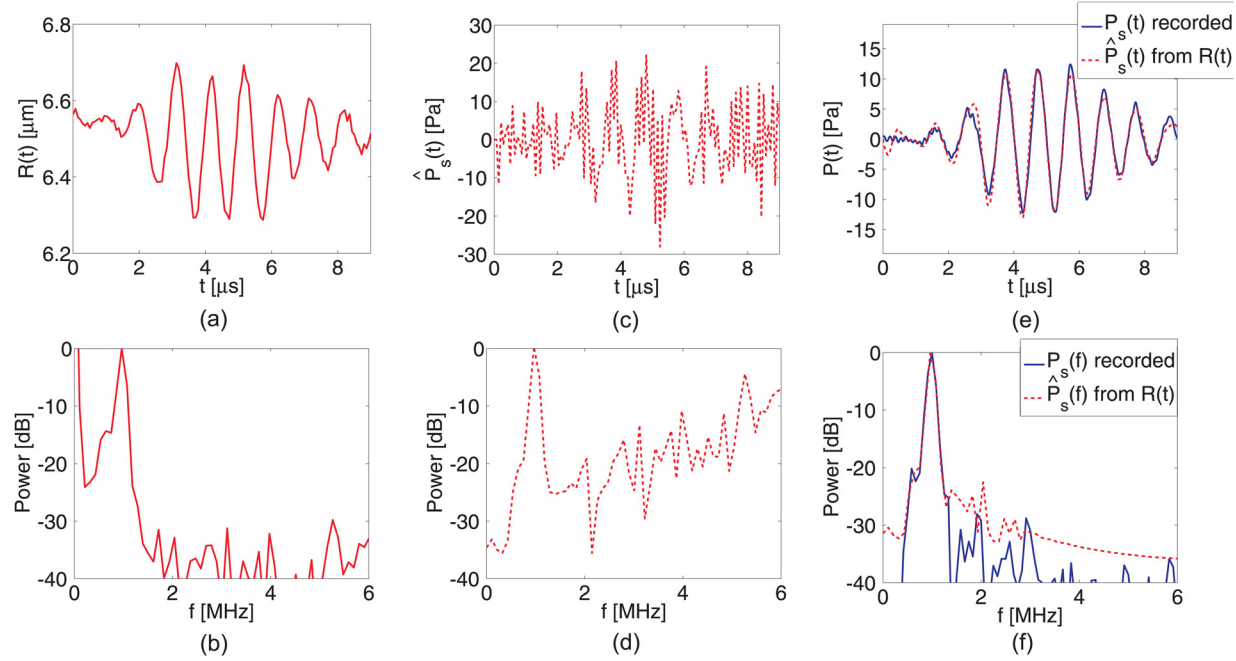


FIG. 5. (Color online) Example of predicted scattered pressure wave from experimentally obtained radial dynamics. The initial bubble radius was  $6.5 \mu\text{m}$ . The driving pressure pulse had a peak amplitude of  $40 \text{ kPa}$  and a frequency of  $1 \text{ MHz}$ . (a) The recorded radial response  $R(t)$ . (b) The power spectrum of the  $R(t)$  curve showing no higher harmonics. (c) Calculated  $\hat{P}_s(t)$  curve with Eq. (1). (d) The power spectrum of the calculated  $\hat{P}_s(t)$  curve. (e) Comparison of the low-pass filtered acoustic response calculated from the  $R(t)$  curve with Eq. (1) (dotted line) and the acoustic response (solid line) measured by the receive transducer. (f) The power spectra of the measured  $P_s(t)$  curve (solid line) and of the low-pass filtered predicted curve (dotted line).

pressure amplitudes from the recorded and the derived pressure traces. The dotted lines in Fig. 6 represent the difference of  $\pm 3 \text{ dB}$  between the two data sets.

The data sets show larger difference in amplitude than presented in Fig. 5(e). Nevertheless, in 65% of the experiments the fundamental response predicted from the  $R(t)$  curve is within  $\pm 3 \text{ dB}$  of the measured fundamental response. In 93% of the experiments the difference is within

$\pm 6 \text{ dB}$ . We observe that the measured fundamental acoustic response is typically  $1 \text{ dB}$  lower than the acoustic response predicted from the  $R(t)$  curve. Several possible causes can be identified for the variation and difference. The first possible cause is the acoustic attenuation of the wall of the cellulose capillary tube, which would lower the measured acoustic response. Second, an error in the determination of the bubble radius,  $R$ , could affect the predicted amplitude in the cubic relation [see Eq. (2)]. Preliminary studies have shown that small differences in optical focusing could result in a systematic measurement error in the radius of 15%. Third is a possible error in the calibration value of the receiving transducer. The hydrophone used as a standard for the calibration has an accuracy of 10%, or  $0.8 \text{ dB}$ , as stated by the manufacturer.

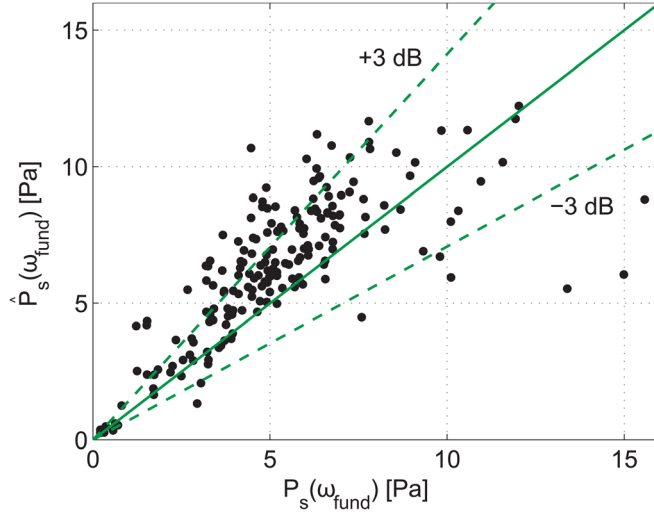


FIG. 6. (Color online) A comparison between the amplitude of the acoustic bubble response at the driving frequency as measured by the receive transducer  $P_s(\omega_{\text{fund}})$  and the acoustic response as predicted from the measured  $R(t)$  curve  $\hat{P}_s(\omega_{\text{fund}})$  for 194 different experiments with 16 different bubbles. The driving pressure amplitude of  $40 \text{ kPa}$  is fixed for all experiments while the driving pressure frequency was varied. The dotted lines represent a  $+3 \text{ dB}$  and  $-3 \text{ dB}$  difference between the two data sets.

## B. Nonlinear response

In the example presented in Fig. 5 the bubble is oscillating linearly, and no signal appears at the higher frequencies. The latter implies that high-frequency noise on the predicted  $\hat{P}_s(t)$  curve can be removed by a low-pass filter without signal loss. However, a bubble oscillating nonlinearly may show higher-harmonic oscillations and the use of a low-pass filter would result in signal loss. Figure 7(a) shows an example of a bubble with a subharmonic oscillation behavior. The bubble has an initial bubble radius of  $4.9 \mu\text{m}$  and it was excited with a driving pulse with a frequency of  $1.8 \text{ MHz}$ . Since the driving frequency was close to twice the eigenfrequency of the encapsulated bubble of  $0.94 \text{ MHz}$ ,<sup>21</sup> the bubble responds nonlinearly with a subharmonic oscillation at a frequency of  $0.9 \text{ MHz}$ . The radial subharmonic response

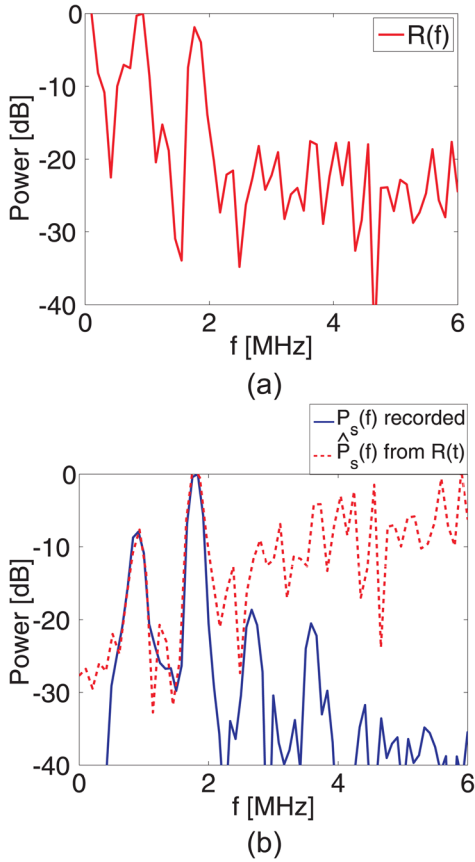


FIG. 7. (Color online) (a) Power spectrum of the radial response of a bubble with an initial radius of  $4.9 \mu\text{m}$ . A subharmonic response is visible at a frequency of  $0.9 \text{ MHz}$ , which is at half the driving frequency of  $1.8 \text{ MHz}$ . (b) The spectrum of the pressure calculated from the  $R(t)$  curve  $\hat{P}_s(f)$  (dotted line) and the pressure measured directly  $P_s(f)$  (solid line).

is higher than the fundamental response at a frequency of  $1.8 \text{ MHz}$ . The resulting acoustic response from these nonlinear oscillations is calculated with Eq. (1). Figure 7(b) shows the power spectrum of the resulting acoustic response which is compared to the power spectrum of the simultaneously measured acoustic response. For the fundamental response and the subharmonic response the agreement is very good. As explained by the  $\omega^2$  dependence in Eq. (2) the subharmonic acoustic response has decreased fourfold, or  $12 \text{ dB}$ , relative to the fundamental acoustic response.

### C. The inverse problem

In the measured acoustic response shown in Fig. 7(b) we observe higher-harmonic content at frequencies of  $2.7$  and  $3.6 \text{ MHz}$ , which is not visible in the radial response, and therefore also not in the pressure response predicted from the radial response. The signal-to-noise ratio (SNR) of  $R(t)$  is about  $25 \text{ dB}$  [Fig. 7(a)]. The SNR of  $P_s(t)$  is about  $40 \text{ dB}$ , thus showing a superior resolving power for higher-harmonic responses and smaller oscillation amplitudes. Moreover, these data, in conjunction with the  $\omega^2$  dependence presented in Eq. (2), suggest that higher-harmonic radial excursions may be better detected from the acoustic recordings. Experimental recording of the acoustic response of a microbubble may thus become complementary to optical

recordings. Inversion of Eq. (1) should then assist in finding the radial dynamics from the experimental pressure–time curve.

Here, we show that it is possible to reconstruct the radial dynamics from the measured  $P_s(t)$  curve. The radial dynamics can be recovered from a double integration of Eq. (1),

$$\hat{R}^3(t) = R^3(0) + \int_0^t \left( 3R^2(0)\dot{R}(0) + \frac{3r}{\rho} \int_0^{t'} P_s(r, s) dt' \right) dt'. \quad (4)$$

The initial bubble radius was obtained from the optical recordings and the initial bubble wall velocity was always taken to be zero ( $\dot{R}(0) = 0$ ). The distance  $r$  between the microbubble and receiving transducer is known for this experimental setup. Finally, the acoustic response is integrated numerically to obtain the bubble radius  $R(t)$  as a function of time. The numerical integration is done with the trapezoidal rule in MATLAB.

In Fig. 8 the result from solving this inverse problem is shown for the acoustic response of the very same bubble as presented in Fig. 5. The bubble had a radius of  $6.5 \mu\text{m}$  and it was subjected to a  $1 \text{ MHz}$  pulse. The measured acoustic response  $P_s(t)$  was numerically integrated twice to give  $\hat{R}^3(t)$ . Noise in the recorded acoustic response gives the  $P_s(t)$  curve a small offset. The double integration is extremely sensitive to low frequencies and a small offset results in a drift and an unphysical growth of the bubble size in the final

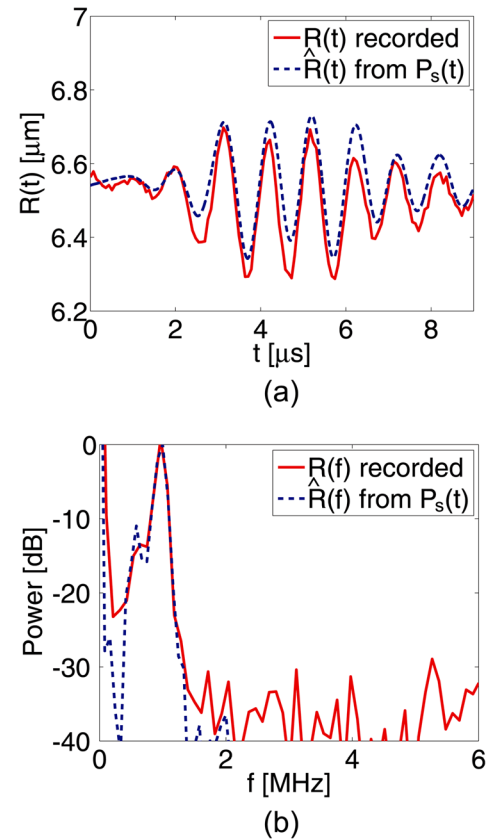


FIG. 8. (Color online) An example of the results obtained with the inverse method. (a) The recorded acoustic response of a  $6.6 \mu\text{m}$  radius bubble; the distance between the focused transducer and the microbubble was  $2.6 \text{ cm}$  [the same as in Fig. 5(a)]. (b) The power spectrum of the signals in (a).

$R(t)$  curve. We corrected for this drift by applying a second order Butterworth 0.2 MHz high-pass filter on  $\dot{R}^3(t)$  after the first integration step. For small time steps ( $\Delta t < 5 \times 10^{-8}$  s) the double integration was found to converge to the predicted  $\hat{R}(t)$  curve as shown in Fig. 8. The good agreement between the predicted and recorded radial dynamics is remarkable. Oscillations of the bubble wall of tens of nanometers are correctly predicted from an acoustic response measured at a distance of 2.6 cm. Note that we can measure changes in the radius with an accuracy of several tenths of a nanometer. The measurement (the observed radius) is the convolution of the optical point-spread function (PSF) with the real radius of the bubble. The PSF does not change during the measurement and therefore the change in the observed radius is due solely to the change in the real radius of the bubble. Moreover, the observed radius is deduced from an area measurement, see van der Meer *et al.*<sup>21</sup>

A small offset in the radial excursion can be observed between the predicted and the measured  $R(t)$  curves. As discussed before, compression-only behavior gives an offset to the mean radius during the oscillation. The offset can be looked upon as a low-frequency component. Since the receive transducer is not sensitive to such low-frequency components it is not detected; conversion from the recorded  $P_s(t)$  into an  $\hat{R}(t)$  will therefore not predict the compression-only behavior either. Note that a similar effect is also present if no high-pass filter to  $\dot{R}^3(t)$  were applied.

In Fig. 9 the power spectrum of an optically recorded  $R(f)$  curve is presented ( $R_0 = 4.9 \mu\text{m}$ ) together with the spectrum of the radial dynamics  $\hat{R}(f)$  as predicted from the measured  $P_s(t)$  curve. The curves are again normalized with a common factor. We can identify a quantitative agreement between the two curves. The higher-harmonic oscillations of the bubble that are invisible in the optically recorded  $R(t)$  curve are clearly visible in the dynamics determined from the recorded acoustic response. Therefore, Fig. 9 confirms the hypothesis that acoustic techniques can be used to study the higher-harmonic radial dynamics of ultrasound contrast

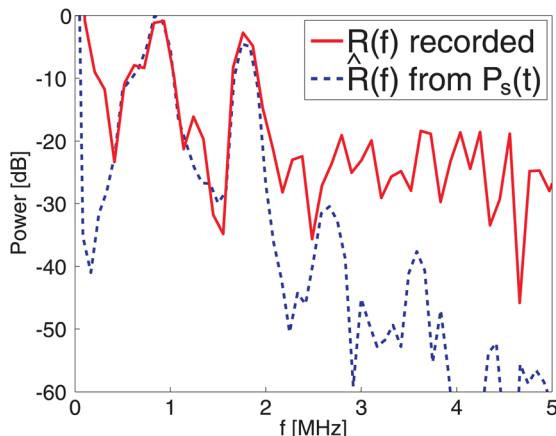


FIG. 9. (Color online) Example of acoustically predicted higher-harmonic radial responses that are not detected optically. The graph shows the power spectra of the  $R(t)$  curves of a bubble with an initial bubble radius of  $4.9 \mu\text{m}$  subjected to a 1.8 MHz pressure pulse [the same response as in Fig. 7(a)]. The noise in the optical data is higher than the levels of the expected higher-harmonic oscillations.

agent microbubbles much more sensitively than the ultra-high-speed camera can.

To investigate the accuracy of the inverse method for all bubble recordings, the amplitudes of the optically recorded radial responses were compared to those of the predicted ones, at the fundamental frequency. The agreement between the two was of similar quality as the one resulting from the agreement seen with the forward method (see Fig. 6) and therefore not plotted. In 60% of the experiments the fundamental response of the radial dynamics predicted from the  $P_s(t)$  curve is within 3 dB of the measured fundamental response. In 80% of the experiments the difference is within 6 dB. The reason for the differences being larger than in the forward method may be the larger sensitivity for the estimate of the bubble radius. On average, the acoustically derived radial response had a slightly lower amplitude of oscillation than the optically observed radial response.

#### D. Surface modes

In some of the conducted experiments nonspherical shape oscillations were observed. The oscillation of these so-called “surface modes” is predominately of period-doubling nature.<sup>42–44</sup> For uncoated bubbles in an unbound medium, Longuet-Higgins has shown that surface modes radiate pressure waves at the subharmonic frequency, with an amplitude that decays with  $1/r^n$ , see Ref. 42, with  $n$  the surface wave mode number. Since the receiving transducer is relatively far from the microbubble, the subharmonic waves scattered by the surface mode oscillations may well be below the noise level. However, the presence of the capillary wall and a nonlinearly behaving coating are violating the boundary conditions set in Ref. 42, namely a free gas bubble in an unbounded fluid. Therefore, it has been hypothesized that surface mode oscillations may contribute to the subharmonic frequency content in the echo. If surface mode oscillations would scatter significant ultrasound waves at the subharmonic frequency then there should be a difference between the subharmonic content calculated from the radius-time curve and the acoustically measured subharmonic content. We have therefore analyzed our data for both the occurrence of subharmonic acoustic emission and the occurrence of surface modes.

Of the set of 16 bubbles a total of 4 bubbles in 23 different experiments showed an acoustic subharmonic response. The threshold for the occurrence of a subharmonic response was set at  $-20$  dB compared to the fundamental-frequency response. Examples of these subharmonic responses are shown in Figs. 4 and 7. The subharmonic emission can also be predicted from the optically measured  $R(t)$  curves. By doing so, we found that the predicted and measured sound emission at the subharmonic frequency overlap within 2.5 dB for 20 of the 23 experiments. Therefore, the occurrence of subharmonic emission can be estimated from the acoustic data as well as from the optical data.

The images were found to be very similar to those recorded earlier by Dollet *et al.*<sup>43</sup> While a very similar decomposition analysis as detailed in Ref. 43 could be utilized to analyze the occurrence of surface modes, here the

images were scored manually. The typical surface mode amplitude grows exponentially over time and in our experiments they reached an amplitude of  $0.3 \mu\text{m}$ , which is of the same order as the volumetric radial oscillations. In 69 cases, surface mode oscillations were visible. Remarkably, in 54 cases the surface mode oscillations were not accompanied by significant subharmonic ultrasound emission, while in the other 15 cases they were. See Table I for the statistics. Moreover, the absence of surface mode oscillations did not predict the occurrence of subharmonic ultrasound emission either. These data suggest that there is no direct correlation between the presence of surface mode oscillations and the presence of subharmonic ultrasound emission in the current experimental settings.

A short note should be addressed to the coupling of period-doubling surface modes to *fundamental* frequency sound emission. Longuet-Higgins<sup>42</sup> predicts that the period-doubling surface modes induce a forcing of the gas volume at the fundamental frequency, which in turn produces an additional fundamental frequency sound emission. Since we are measuring the radial dynamics directly, this possible contribution of the surface modes is already contained in  $R(t)$  and we cannot distinguish the contribution of the surface mode from the contribution of the driving pressure wave.

Surface modes may still play a role in the initiation of volumetric subharmonic oscillations. Furthermore, the optical plane of the microscope is parallel to the wall, and any nonspherical modes with an orientation normal to the wall will not be visible in the optical images.<sup>35</sup> Therefore, a more detailed investigation of the sound emission of surface modes requires a “side view” microscope to visualize the nonspherical modes of the bubble normal to the wall.<sup>35</sup>

## V. DISCUSSION

### A. Noise, sensitivity, and bandwidth

The summarized results presented in Fig. 6 show that Eq. (1) can be used to predict the scattered sound from the recording of radial dynamics. Sound levels on the order of 1 Pa could be detected and predicted using both optical and acoustical techniques. The inverse method, predicting the radial dynamics from the echo, also shows good correlation between the predicted and recorded radial dynamics. For a single bubble, the difference between predicted and measured time traces can be large, up to a factor of 3. We have suggested that both noise and calibration play a major role in the observed differences. The influence of both is further discussed in this section.

The examples of acoustic measurements presented in Figs. 7(b) and 9 show a signal level of about 10 Pa and a noise level of about 0.1 Pa (SNR  $\sim 40$  dB). For equal relative radial excursion and frequency the echo amplitude grows

TABLE I. Overview of occurrence of subharmonic scattering and surface modes. Total number of recordings is 192.

	Acoustic subharmonic	No acoustic subharmonic
Surface modes	15	54
No surface modes	8	115

with the third power of the radius [see Eq. (2)], while noise in the receiving system is independent of the radius. Therefore, the SNR will decrease dramatically in acoustic recordings of smaller microbubbles. On the other hand, it can be shown that noise in the optical recordings is inversely proportional to the bubble radius because of the finite pixel size of the CCD sensor (with the  $100\times$  objective the resolution is  $\sim 0.20 \mu\text{m}/\text{pixel}$ ). Therefore, the SNR decreases also in optical recordings of smaller bubbles, although to a lesser extent. We found that the acoustic recordings of the smallest bubbles in our data set ( $R_0 < 2 \mu\text{m}$ ) show a SNR of about 20–30 dB while the optical recordings have a SNR of about 10 dB or worse. Thus, the acoustic recordings show an overall higher SNR than the optical recordings.

The  $\omega^2$  dependence in the conversion from radial dynamics to a pressure wave implies that acoustical methods are more sensitive to detect higher-harmonic emission. This is demonstrated in Fig. 9, in which the higher-harmonic *radial* dynamics were not detected by optical recordings but only through acoustical recordings. The  $\omega^2$  dependence also implies that optical methods are more sensitive to detect subharmonic emission. This effect is visible in, for example, Fig. 7. Strictly speaking, the high acoustical sensitivity is only present in a limited frequency band. The transducer has a frequency band of about 1–5 MHz and outside this range the SNR is much lower. Therefore, low-frequency features of the radial dynamics such as compression-only behavior might not be captured by the present transducer. In future experiments this drawback could be worked around by the addition of a dedicated low-frequency transducer. Transducers such as hydrophones that have much larger bandwidth also generally have higher noise levels and therefore may not be able to detect pressure levels of 1–10 Pa with sufficient SNR. The Branderis 128 ultra-high-speed camera has an effective bandwidth of 0–12.5 MHz when operated at its maximum frame rate and can therefore inherently capture the low-frequency contents.

The sensitivity of the optically recorded radial response could be improved. One could try to increase the optical zoom to decrease the influence of the finite pixel size. Another improvement would be to reduce motion blur of the oscillating bubble wall by decreasing the exposure times within the design of the Branderis-128 camera. This also requires either more sensitive CCDs or an increased intensity of the illumination. A third option would be to use laser-induced fluorescence techniques and high-intensity illumination to increase the contrast of the bubble wall with respect to the background illumination. Finally, improved data processing of the images may lead to noise reduction in the  $R(t)$  curves. The  $R(t)$  curves are derived from a simple minimum cost algorithm applied to the derivative of the grayscale values in the image, to determine the contour of the bubble. However, no sophisticated preprocessing has been applied until now. Edge enhancement and noise reduction algorithms could lead to  $R(t)$  curves with a significantly reduced noise level.

With respect to the calibration of the receiving transducer it may be concluded from the good data agreement that the calibration procedure suffices. However, time trace analysis of the recorded and predicted echoes sometimes

show a different trace despite a good agreement in the frequency domain of the two signals. Analysis showed that this was caused by the frequency-dependent phase response of the receiving transducer and subsequent acquisition system. The phase response produces a different delay of the various frequency components in the recorded acoustic signal. The optical system has an almost frequency-independent phase response and therefore a difference in the time trace between the recorded and predicted time traces can be expected. A future setup may benefit from the calibration of the phase response of the receiving transducer as suggested by van Neer *et al.*<sup>45</sup>

It is convenient to use the linearized form Eq. (2) instead of the nonlinear equation, Eq. (1), since the frequency spectra of radius and pressure are related to each other only through  $\omega^2$ . The data shown in Fig. 5 can be used to exemplify this. A bubble with a radius of  $6.5 \mu\text{m}$  oscillates at a frequency of 1 MHz with a radial amplitude of  $0.2 \mu\text{m}$  [Fig. 5(a)] and produces a 1 MHz pressure amplitude of 12.5 Pa at a distance of 2.6 cm [Fig. 5(e)], well in line with what is predicted with Eq. (2). While this may work well for the fundamental response at small amplitudes of oscillations, a note of caution is in order here. A nonlinear second harmonic signal can be picked up in the acoustic response, see, e.g., Figs. 5(f) and 7. To what extent these nonlinear contributions originate from the nonlinear Rayleigh–Plesset equation, including a potentially nonlinear description of the bubble shell, or from Eq. (1) is not clear *a priori*. The higher order harmonics in the scattered signal may arise from a nonlinear conversion from a linear response  $R(t)$  to  $P_s(t)$ , necessitating the use of Eq. (1). Conversely, a nonlinear acoustic response could be calculated from a nonlinear radial response through Eq. (2). The optical sensitivity near the second harmonic frequency was limited to  $-40 \text{ dB}$  and made an experimental interpretation of the exact origin of the nonlinear contributions in the acoustic response rather inconclusive. These are interesting subjects for future numerical investigations.

## B. Remote acoustic detection of radial dynamics

The inverse acoustic method may have advantages over optical recordings in *in vitro* studies of the radial dynamics of ultrasound contrast agent microbubbles, in addition to the higher SNR. Optical recordings with a microscope inherently need an objective mounted close to the bubble, regularly at a distance on the order of 1 mm. Such an objective may produce acoustic reflections that interfere with the bubble signals. Acoustic recordings can be performed remotely, at a distance of 10 cm or more from the bubble. A disadvantage of the acoustical method is the precarious isolation of single microbubbles, a requirement less stringent in the optical microscope method.

The inverse method could potentially provide a new tool to investigate the relation between local mechanical action and enhanced drug uptake by cells<sup>11,12,46</sup> *in vivo*. In literature it is suggested that strain caused by oscillating bubbles close to a cell membrane results in opening of the cell and enhanced drug uptake. Strain could be estimated from the oscillation amplitude of the bubble.<sup>12,46–48</sup> Thus, in the

future a remote acoustic detection method may give direct feedback on the locally controlled mechanical forcing near cells. One requirement for such an application is to know the initial bubble radius to enable the integration of Eq. (4). Acoustic techniques based on off-resonant bubble sizing<sup>49–51</sup> or optical techniques based on laser light scattering<sup>52</sup> could provide an estimate of the initial bubble radius. More elegantly, the size requirement could be fulfilled by the use of monodisperse ultrasound contrast agent microbubbles that can be produced through flow focusing in a lab-on-a-chip device.<sup>53,54</sup>

## VI. CONCLUSIONS

In conclusion, we have experimentally shown that the radial dynamics of an isolated oscillating microbubble can be used to predict its acoustic emission. It is shown that higher order harmonics in the radial dynamics of the microbubbles are enhanced in the acoustic emission. Conversely, the measured acoustic emission resulting from an isolated oscillating microbubble with a known initial bubble radius can be converted to correctly describe the radial bubble dynamics. Ultra-high-speed imaging and acoustic recordings are shown to complement each other in the characterization of both the dynamic and the acoustic behavior of ultrasound contrast agent microbubbles. Small amplitude behavior and the higher-harmonic response is shown to be characterized more sensitively by acoustic techniques. Nonspherical oscillations and low-frequency behavior such as compression-only behavior, which are important features in modeling and predicting bubble behavior, are exclusively captured in the optical configuration.

## ACKNOWLEDGMENTS

We wish to thank Benjamin Dollet, Marlies Overvelde, Valeria Garbin, and Peter Frinken for fruitful discussions. We gratefully acknowledge Gert-Wim Bruggert and Martin Bos for their skillful technical assistance. Bracco Research S.A., Geneva, Switzerland, is acknowledged for providing the experimental contrast agent BR-14.

<sup>1</sup>J. Lindner, “Microbubbles in medical imaging: Current applications and future directions,” *Nat. Rev. Drug Discovery* **3**, 527–533 (2004).

<sup>2</sup>S. Hilgenfeldt, D. Lohse, and M. Zomack, “Response of bubbles to diagnostic ultrasound: A unifying theoretical approach,” *Eur. Phys. J.* **4**, 247–255 (1998).

<sup>3</sup>V. Mor-Avi, E. Caiani, K. Collins, C. Korcarz, J. Bednarz, and R. Lang, “Combined assessment of myocardial perfusion and regional left ventricular function by analysis of contrast-enhanced power modulation images,” *Circulation* **104**, 352–357 (2001).

<sup>4</sup>D. H. Simpson, C. Chin, and P. Burns, “Pulse inversion Doppler: A new method for detecting nonlinear echoes from microbubble contrast agents,” *IEEE Trans. Ultrason. Ferroelectr. Freq. Control* **46**, 372–382 (1999).

<sup>5</sup>J. E. Chomas, P. A. Dayton, D. J. May, and K. W. Ferrara, “Nondestructive subharmonic imaging,” *IEEE Trans. Ultrason. Ferroelectr. Freq. Control* **49**, 883–892 (2002).

<sup>6</sup>G. Bhagavatheeeshwaran, W. T. Shi, F. Forsberg, and P. M. Shankar, “Subharmonic signal generation from contrast agents in simulated neovessels,” *Ultrasound Med. Biol.* **30**, 199–203 (2004).

<sup>7</sup>D. Goertz, M. Frijlink, D. Tempel, V. Bhagwandas, A. Gisolf, R. Kram, N. de Jong, and A. van der Steen, “Subharmonic contrast intravascular ultrasound for vasa vasorum imaging,” *Ultrasound Med. Biol.* **33**, 1859–1872 (2007).

- <sup>8</sup>P. J. A. Frinking, E. Gaud, J. Brochot, and M. Ardit, "Subharmonic scattering of phospholipid-shell microbubbles at low acoustic pressure amplitudes," *IEEE Trans. Ultrason. Ferroelectr. Freq. Control* **57**, 1762–1771 (2010).
- <sup>9</sup>J. Sijl, B. Dollet, M. Overvelde, V. Garbin, T. Rozendal, N. de Jong, D. Lohse, and M. Versluis, "Subharmonic behavior of phospholipid-coated microbubbles," *J. Acoust. Soc. Am.* **128**, 3239–3252 (2010).
- <sup>10</sup>S. B. Feinstein, "The powerful microbubble: From bench to bedside, from intravascular indicator to therapeutic delivery system, and beyond," *Am. J. Physiol. Heart Circ. Physiol.* **287**, H450–457 (2004).
- <sup>11</sup>A. van Wamel, K. Kooiman, M. Harteveld, M. Emmer, F. J. ten Cate, M. Versluis, and N. de Jong, "Vibrating microbubbles poking individual cells: Drug transfer into cells via sonoporation," *J. Controlled Release* **112**, 149–155 (2006).
- <sup>12</sup>C. D. Ohl, M. Arora, R. Ikink, N. de Jong, M. Versluis, M. Delius, and D. Lohse, "Sonoporation from jetting cavitation bubbles," *Biophys. J.* **91**, 4285–4295 (2006).
- <sup>13</sup>J. W. Rayleigh, "On the pressure developed in a liquid during the collapse of a spherical cavity," *Philos. Mag.* **34**, 94–98 (1917).
- <sup>14</sup>T. G. Leighton, *The Acoustic Bubble* (Academic, London, 1994), Chap.4, pp. 287–430.
- <sup>15</sup>M. P. Brenner, S. Hilgenfeldt, and D. Lohse, "Single-bubble sonoluminescence," *Rev. Mod. Phys.* **74**, 425–483 (2002).
- <sup>16</sup>A. Prosperetti, "Nonlinear oscillations of gas bubbles in liquids. transient solutions and the connection between subharmonic signal and cavitation," *J. Acoust. Soc. Am.* **57**, 810–821 (1975).
- <sup>17</sup>N. de Jong, A. Bouakaz, and P. J. A. Frinking, "Basic acoustic properties of microbubbles," *Echocardiogr.* **19**, 229–240 (2002).
- <sup>18</sup>P. Marmottant, S. M. van der Meer, M. Emmer, M. Versluis, N. de Jong, S. Hilgenfeldt, and D. Lohse, "A model for large amplitude oscillations of coated bubbles accounting for buckling and rupture," *J. Acoust. Soc. Am.* **118**, 3499–3505 (2005).
- <sup>19</sup>A. A. Doinikov and P. A. Dayton, "Maxwell rheological model for lipid-shelled ultrasound microbubble contrast agents," *J. Acoust. Soc. Am.* **121**, 3331–3340 (2007).
- <sup>20</sup>M. Emmer, A. van Wamel, D. Goertz, and N. de Jong, "The onset of microbubble vibration," *Ultrasound Med. Biol.* **33**, 941–949 (2007).
- <sup>21</sup>S. van der Meer, B. Dollet, M. Voormolen, C. Chin, A. Bouakaz, N. de Jong, M. Versluis, and D. Lohse, "Microbubble spectroscopy of ultrasound contrast agents," *J. Acoust. Soc. Am.* **121**, 648–656 (2007).
- <sup>22</sup>J. Sijl, E. Gaud, P. J. A. Frinking, M. Ardit, N. de Jong, D. Lohse, and M. Versluis, "Acoustic characterization of single ultrasound contrast agent microbubbles," *J. Acoust. Soc. Am.* **124**, 4091–4097 (2008).
- <sup>23</sup>E. Stride, "The influence of surface adsorption on microbubble dynamics," *Philos. Trans. R. Soc. London, Ser. A* **366**, 2103–2115 (2008).
- <sup>24</sup>K. Chetty, E. Stride, C. A. Sennoga, J. V. Hajnal, and R. J. Eckersley, "High-speed optical observations and simulation results of SonoVue microbubbles at low-pressure insonation," *IEEE Trans. Ultrason. Ferroelectr. Freq. Control* **55**, 1333–1342 (2008).
- <sup>25</sup>M. Emmer, H. J. Vos, and N. de Jong, "Radial modulation of single microbubbles," *IEEE Trans. Ultrason. Ferroelectr. Freq. Control* **56**, 2370–2379 (2009).
- <sup>26</sup>J. Tu, J. Guan, Y. Qiu, and T. J. Matula, "Estimating the shell parameters of SonoVue microbubbles using light scattering," *J. Acoust. Soc. Am.* **126**, 2954–2962 (2009).
- <sup>27</sup>M. Overvelde, V. Garbin, J. Sijl, B. Dollet, N. de Jong, D. Lohse, and M. Versluis, "Nonlinear shell behavior of phospholipid-coated microbubbles," *Ultrasound Med. Biol.* **36**, 2080–2092 (2010).
- <sup>28</sup>K. E. Morgan, J. S. Allen, P. A. Dayton, J. E. Thomas, A. L. Klibanov, and K. W. Ferrara, "Experimental and theoretical evaluation of microbubble behavior: Effect of transmitted phase and bubble size," *IEEE Trans. Ultrason. Ferroelectr. Freq. Control* **47**, 1494–1509 (2000).
- <sup>29</sup>A. A. Doinikov, S. Zhao, and P. A. Dayton, "Modeling of the acoustic response from contrast agent microbubbles near a rigid wall," *Ultrasonics* **49**, 195–201 (2009).
- <sup>30</sup>P. A. Frost and E. Y. Harper, "Acoustic radiation from surfaces oscillating at large amplitude and small Mach number," *J. Acoust. Soc. Am.* **58**, 318–325 (1975).
- <sup>31</sup>J. R. Lindner, J. Song, A. R. Jayaweera, J. Sklenar, and S. Kaul, "Microvascular rheology of Definity microbubbles after intra-arterial and intravenous administration," *J. Am. Soc. Echocardiogr.* **15**, 396–403 (2002).
- <sup>32</sup>S. Zhao, K. W. Ferrara, and P. A. Dayton, "Asymmetric oscillation of adherent targeted ultrasound contrast agents," *Appl. Phys. Lett.* **87**, 134103 (2005).
- <sup>33</sup>V. Garbin, D. Cojoc, E. Ferrari, E. Di Fabrizio, M. L. J. Overvelde, S. M. van der Meer, N. de Jong, D. Lohse, and M. Versluis, "Changes in microbubble dynamics near a boundary revealed by combined optical micromanipulation and high-speed imaging," *Appl. Phys. Lett.* **90**, 114103 (2007).
- <sup>34</sup>C. F. Caskey, S. M. Stieger, S. Qin, P. A. Dayton, and K. W. Ferrara, "Direct observations of ultrasound microbubble contrast agent interaction with the microvessel wall," *J. Acoust. Soc. Am.* **122**, 1191–1200 (2007).
- <sup>35</sup>H. J. Vos, B. Dollet, J. G. Bosch, M. Versluis, and N. de Jong, "Nonspherical vibrations of microbubbles in contact with a wall—A pilot study at low mechanical index," *Ultrasound Med. Biol.* **34**, 685–688 (2008).
- <sup>36</sup>C. T. Chin, C. Lancée, J. M. G. Borsboom, F. Mastik, M. E. Frijlink, N. de Jong, M. Versluis, and D. Lohse, "Brandaris 128: A digital 25 million frames per second camera with 128 highly sensitive frames," *Rev. Sci. Instrum.* **74**, 5026–5034 (2003).
- <sup>37</sup>K. Vokurka, "On Rayleigh's model of a freely oscillating bubble. I. Basic relations," *Czech. J. Phys. Sect. B* **35**, 28–40 (1985).
- <sup>38</sup>V. Garbin, B. Dollet, M. Overvelde, D. Cojoc, E. Di Fabrizio, L. van Wijngaarden, A. Prosperetti, N. de Jong, D. Lohse, and M. Versluis, "History force on coated microbubbles propelled by ultrasound," *Phys. Fluids* **21**, 092003 (2009).
- <sup>39</sup>D. H. Kim, M. Costello, P. Duncan, and D. Needham, "Mechanical properties and microstructure of polycrystalline phospholipid monolayer shells: Novel solid microparticles," *Langmuir* **19**, 8455–8466 (2003).
- <sup>40</sup>N. de Jong, M. Emmer, C. Chin, A. Bouakaz, F. Mastik, D. Lohse, and M. Versluis, "'Compression-only' behavior of phospholipid-coated contrast bubbles," *Ultrasound Med. Biol.* **33**, 653–656 (2007).
- <sup>41</sup>J. Sijl, M. Overvelde, B. Dollet, V. Garbin, N. de Jong, D. Lohse, and M. Versluis, "'Compression-only' behavior: A second order nonlinear response of ultrasound contrast agent microbubbles," *J. Acoust. Soc. Am.* **129**, 1729–1739 (2011).
- <sup>42</sup>M. S. Longuet-Higgins, "Monopole emission of sound by asymmetric bubble oscillations. Part 1. Normal modes," *J. Fluid Mech.* **201**, 525–542 (1989).
- <sup>43</sup>B. Dollet, S. van der Meer, V. Garbin, N. de Jong, D. Lohse, and M. Versluis, "Nonspherical oscillations of ultrasound contrast agent microbubbles," *Ultrasound Med. Biol.* **34**, 1465–1473 (2008).
- <sup>44</sup>M. Versluis, D. Goertz, P. Palanchon, I. L. Heitman, S. M. van der Meer, B. Dollet, N. de Jong, and D. Lohse, "Microbubble shape oscillations excited through ultrasonic parametric driving," *Phys. Rev. E* **82**, 026321 (2010).
- <sup>45</sup>P. L. M. J. van Neer, H. J. Vos, and N. de Jong, "Reflector-based phase calibration of ultrasound transducers," *Ultrasonics* **51**, 1–6 (2011).
- <sup>46</sup>P. Marmottant and S. Hilgenfeldt, "Controlled vesicle deformation and lysis by single oscillating bubbles," *Nature (London)* **423**, 153–156 (2003).
- <sup>47</sup>P. Prentice, A. Cuschieri, K. Dholokia, M. Prausnitz, and P. Campbell, "Membrane disruption by optically controlled microbubble cavitation," *Nat. Phys.* **148**, 1–4 (2005).
- <sup>48</sup>X. Liu and J. Wu, "Acoustic microstreaming around an isolated encapsulated microbubble," *J. Acoust. Soc. Am.* **125**, 1319–1330 (2009).
- <sup>49</sup>H. Medwin, "Counting bubbles acoustically: A review," *Ultrasonics* **15**, 7–13 (1977).
- <sup>50</sup>A. D. Phelps and T. G. Leighton, "High-resolution bubble sizing through detection of the subharmonic response with a two-frequency excitation technique," *J. Acoust. Soc. Am.* **99**, 1985–1992 (1996).
- <sup>51</sup>D. Maresca, M. Emmer, P. van Neer, H. Vos, M. Versluis, M. Muller, N. de Jong, and A. van der Steen, "Acoustic sizing of an ultrasound contrast agent," *Ultrasound Med. Biol.* **36**, 1713–1721 (2010).
- <sup>52</sup>J. Guan and T. J. Matula, "Using light scattering to measure the response of individual ultrasound contrast microbubbles subjected to pulsed ultrasound *in vitro*," *J. Acoust. Soc. Am.* **116**, 2832–2842 (2004).
- <sup>53</sup>K. Hettiarachchi, E. Talu, M. L. Longo, P. A. Dayton, and A. P. Lee, "On-chip generation of microbubbles as a practical technology for manufacturing contrast agents for ultrasonic imaging," *Lab on a Chip* **7**, 463–468 (2007).
- <sup>54</sup>B. Dollet, W. van Hoeve, J. P. Raven, P. Marmottant, and M. Versluis, "Role of the channel geometry on the bubble pinch-off in flow-focusing devices," *Phys. Rev. Lett.* **100**, 034504 (2008).